Fatigue Performance of a Lightweight Composite Bridge Deck with Open Ribs

Shihong Zhang[1]; Xudong Shao, Ph.D.[2]; Junhui Cao[3]; Jianfeng Cui[4]; Jianhua Hu, Ph.D., M.ASCE[5]; and Lu Deng, Ph.D., M.ASCE[6]

Abstract: An innovative lightweight composite deck (LWCD) is proposed for steel bridges to avoid premature fatigue cracking. The composite deck is composed of an open-ribbed orthotropic steel deck (OSD) and a thin ultrahigh-performance concrete (UHPC) layer. This study is based on a suspension steel bridge in China, namely, the Second Dongting Lake Bridge. The following investigations were performed: (1) preliminary finite-element analysis (FEA) was carried out to evaluate the vehicle-induced stress ranges (i.e., $\Delta\sigma = \sigma_{\max} - \sigma_{\min}$) of six typical fatigue-prone details; (2) parameter analyses were performed to investigate the effects of the shape of cutouts and the thickness of the floor beams; and (3) two fatigue tests, one that used a full-scale LWCD panel and another that used a LWCD beam specimen, were conducted to reveal fatigue performance of the OSD and the stud shear connectors, respectively. Results of the preliminary FEA show that, with the contribution of the UHPC layer, the vehicle-induced stress ranges at some fatigue details of the LWCD, such as the rib–deck plate welded joints and the splice welds of the longitudinal ribs, were reduced to be less than their constant-amplitude fatigue limits, which indicates theoretically infinite fatigue lives of these details. The parameter analyses reveal that the apple-shaped cutout had relative good fatigue properties among the four cutout schemes and that the thickness of the floor beams is recommended to be 14–18 mm. According to the fatigue tests on the composite panel specimen and on the composite beam specimen, both the open-ribbed OSD and the stud shear connectors exhibited satisfactory fatigue endurances, which were much greater than 2 million cycles. The current theoretical and experimental investigations reveal that the proposed open-ribbed LWCD has favorable fatigue performances. **DOI: 10.1061/(ASCE)BE.1943-5592.0000905.**

Author keywords: Orthotropic steel deck (OSD); Open rib; Ultrahigh-performance concrete (UHPC); Lightweight composite deck (LWCD); Hot spot stress; Fatigue test.

Introduction

Orthotropic steel decks (OSDs) have become standard components for long-span steel bridges because of their advantages, such as high capacities, light self-weight, and convenience in erection (Xiao et al. 2008). However, because of complex factors related to design, construction, and maintenance, some OSD bridges are subjected to premature fatigue cracks under cyclic traffic loads (Jong 2004).

To address these issues, the authors propose a composite deck system for OSD bridges (Shao et al. 2013). The new composite deck is composed of an OSD and a thin ultrahigh-performance concrete (UHPC) layer, with the two components connected through stud shear connectors. Considering that the UHPC layer usually has a thickness of only approximately 50 mm, the OSD–UHPC composite deck is also referred to as a lightweight composite deck (LWCD).

Extensive research has been carried out to reveal the basic performance of LWCDs (Shao et al. 2013; Ding and Shao 2015; Cao et al. 2015). Ding and Shao (2015) compared the stresses in a conventional close-ribbed OSD and a LWCD through finite-element analysis (FEA), which was based on the hot spot stress method. The results showed that the thin UHPC layer significantly reduced vehicle-induced stresses in the OSD. As a result, the stress ranges at some fatigue-prone details in the LWCD were below their constant-amplitude fatigue limits (CAFLs). Thus, the risk of fatigue cracking in the LWCD should be reduced significantly. However, the authors also observed that the stress reductions at the rib–floor beam joints were less apparent, which indicates that the fatigue cracking risk still exists at the rib–floor beam welded joints in the LWCD with U-shaped ribs.

Much research has been performed to explore the fatigue behavior of rib–floor beam weld joints and the free edge of the cutouts in floor beams. Results of studies by Connor (2004) indicated that, among different configuration schemes related to the depth and width of the cutouts, the most favorable cutout shapes on floor beams have the following characteristics: (1) the cutout should start from 1/3 to 1/2 the depth of U-shaped ribs; (2) vertical cuts should

[1]Assistant Engineer, Henan Provincial Communications Planning, Survey and Design Institute Co., Ltd., Zhengzhou 450015, China; Formerly, Graduate Student, Key Laboratory for Wind and Bridge Engineering of Hunan Province, Hunan Univ., Changsha 410082, China. E-mail: 18229973845@163.com

[2]Professor, Key Laboratory for Wind and Bridge Engineering of Hunan Province, Hunan Univ., Changsha 410082, China. E-mail: shaoxd@hnu.edu.cn

[3]Ph.D. Candidate, Key Laboratory for Wind and Bridge Engineering of Hunan Province, Hunan Univ., Changsha 410082, China (corresponding author). E-mail: caojunhui@hnu.edu.cn

[4]Senior Engineer, Hunan Provincial Communications Planning, Survey and Design Institute, Changsha 410008, China. E-mail: cuijianfeng@hnjtsjy.com

[5]Senior Engineer, Hunan Provincial Communications Planning, Survey and Design Institute, Changsha 410008, China. E-mail: hujianhua@hnjtsjy.com

[6]Professor, Key Laboratory for Wind and Bridge Engineering of Hunan Province, Hunan Univ., Changsha 410082, China. E-mail: denglu@hnu.edu.cn

Note. This manuscript was submitted on June 4, 2015; approved on December 10, 2015; published online on February 19, 2016. Discussion period open until July 19, 2016; separate discussions must be submitted for individual papers. This paper is part of the ***Journal of Bridge Engineering***, © ASCE, ISSN 1084-0702.

be used; and (3) cutout should have 50- to 75-mm transition radii at the top. Connor and Fisher (2006) proposed that it was beneficial to add backing plates to the inner space of the U-shaped ribs, because the local stiffness at the rib–floor beam joints could be enhanced. Erzurumlu and Toprac (1972) found that it was favorable to increase the radius of the cutout in the web of the floor beams because it improved the fatigue performance of the free edge of the cutouts.

The previously mentioned research, all related to OSDs with close ribs, is widely used in modern days. However, studies by Wolchuk (1999) and Wolchuk and Ostapenko (1992) revealed that OSDs with open ribs display better fatigue properties. Results of their studies indicate that, in OSDs with open ribs, the local secondary stresses at the rib–floor beam weld joints are eliminated because of simple connections. In addition, open ribs are more convenient in fabrication, installation, and welding (Wolchuk 1999). Frýba and Gajdos (1999) carried out a series of fatigue tests on open-ribbed orthotropic decks, and the results show that apple-shaped cutouts have better stress distributions than circle-shaped cutouts when only bending effects are considered.

Considering the aforementioned advantages of open-ribbed OSDs, the authors propose an innovative open-ribbed LWCD composed of a thin UHPC layer and an OSD with bulb flat open ribs. The research in this paper was aimed at revealing the fatigue characteristics of open-ribbed LWCDs; this research included the following: (1) FEA performed to explore unfavorable fatigue-prone details in the open-ribbed LWCD; (2) parametric analyses conducted on the unfavorable fatigue-prone details that were determined from Step (1), namely, the rib–floor beam weld joints and the free edges of the cutouts; and (3) two fatigue tests carried out for the open-ribbed LWCD. The tests consisted of two specimens. One was a composite deck panel specimen, and the other was a composite beam specimen; these specimens were used to reveal the fatigue performance of the OSD and the stud shear connectors, respectively. The fatigue tests revealed that the open-ribbed LWCD has reliable fatigue endurance. The theoretical and experimental studies discussed in this paper reflect that the open-ribbed LWCD is a favorable deck alternative for OSD bridges.

Brief Introduction to the Second Dongting Lake Bridge

The Second Dongting Lake (SDTL) Bridge in China was used as an example in the present study. The SDTL Bridge spans Dongting Lake, the second largest freshwater lake in China. The SDTL Bridge is a two-pylon two-span steel truss girder suspension bridge with a main span length of 1,480 m. The steel truss girder has a depth of 9.0 m and a width of 35.4 m, and it provides six traffic lanes in two directions. The truss girder of the bridge is divided into 115 constructional segments. The main cable of the bridge has a sag ratio of 1/10. The suspenders are spaced 16.8–17.6 m along the driving direction and are spaced 35.4 m along the transversal direction. To date, the SDTL Bridge is still under construction.

To prevent the OSDs from premature fatigue cracking, a LWCD system is proposed for the SDTL Bridge (Fig. 1). The proposed composite deck consists of an open-ribbed OSD and a 50-mm-thick UHPC layer.

The OSD component was designed as a 12-mm-thick steel deck plate stiffened with HP260 × 12 (height × thickness) longitudinal bulb flat ribs. The longitudinal ribs have 500-mm center spacing. The deck is supported on the transverse floor beams every 2.8 m. There are two types of floor beams, namely, cross beams and cross ribs. The average depths of the cross beams and cross ribs are 1.38 and 0.75 m, respectively. In the preliminary design, the floor beams were 10 mm thick and had apple-shaped cutouts on their webs [Figs. 1(b–d)].

The UHPC layer is compact reinforced with steel meshes. The steel meshes have a diameter of 10 mm and are spaced 37.5 × 37.5 mm (longitudinal × transversal). The yield strength of the steel meshes is 400 MPa. The steel meshes can increase the tensile strength of the reinforced UHPC significantly. According to studies by Shao et al. (2013), UHPC reinforced with 50- × 50-mm (longitudinal × transversal) steel meshes has a flexural tensile cracking strength of 42.7 MPa.

To provide a robust connection between the OSD and the UHPC layer, stud shear connectors were used at the OSD–UHPC interface. The stud shear connectors have a diameter of 13 mm and a height of 35 mm and are spaced at 125 × 125 mm (longitudinal × transversal).

FEA

To reveal the stresses in the OSD of the SDTL Bridge, two OSD schemes were compared on the basis of FEA, i.e., the conventional OSD [Fig. 1(c)] and the proposed LWCD system [Fig. 1(d)]. In simulating the conventional OSD scheme [Fig. 1(c)], only the OSD was simulated. For the proposed LWCD scheme [Fig. 1(d)], the 50-mm UHPC layer was taken into account because it is a structural component in the LWCD, and the sliding effects between the UHPC and the OSD were also considered.

Methodology

Typical fatigue-prone details in the OSD are categorized as follows (Jong 2004): (1) the rib–deck welded joints, including Details 1 and 2; (2) the rib–floor beam weld joints and the free edge of the cutouts, including Details 3–5; and (3) the butt welds of the longitudinal ribs, including Detail 6, as shown in Fig. 2.

Fatigue evaluation methods, such as the nominal stress and hot spot stress methods, are widely used for steel bridges (Fricke 2003), in which the hot spot method is more suitable for complex welded connections. According to International Institute of Welding recommendations (Hobbacher 2008), in a welded joint, the hot spot points are referred to as the critical points at which the fatigue cracks are most likely to initiate and propagate (Fig. 3).

The hot spot stresses can be captured via FEA. The finite-element models can be built by using either shell elements or solid elements, and the welds can be simulated alternatively. According to studies by Aygül et al. (2012), in hot spot stress evaluation, solid finite-element models, in which it can be considered that the welds yield better agreement with the test results, were compared to shell finite-element models without considering welds, and the former was recommended in the FEA.

Surface-stress extrapolations are typically used to determine hot spot stresses. The commonly used methods include the linear and the quadratic surface-stress extrapolation methods, which are based on two and three reference points, respectively (Hobbacher 2008). In this paper, the quadratic extrapolation method was adopted.

In terms of the six fatigue-prone details presented in Fig. 2, both the nominal stress method and the hot spot stress method were used. The hot spot stress method was used for Details 1–4 with the consideration that they are weld-related details. For Detail 5, the nominal stress method was used because it is a weld-free detail. Although Detail 6 is also a weld-related detail, the nominal stress method was used for it because no structural discontinuities existed.

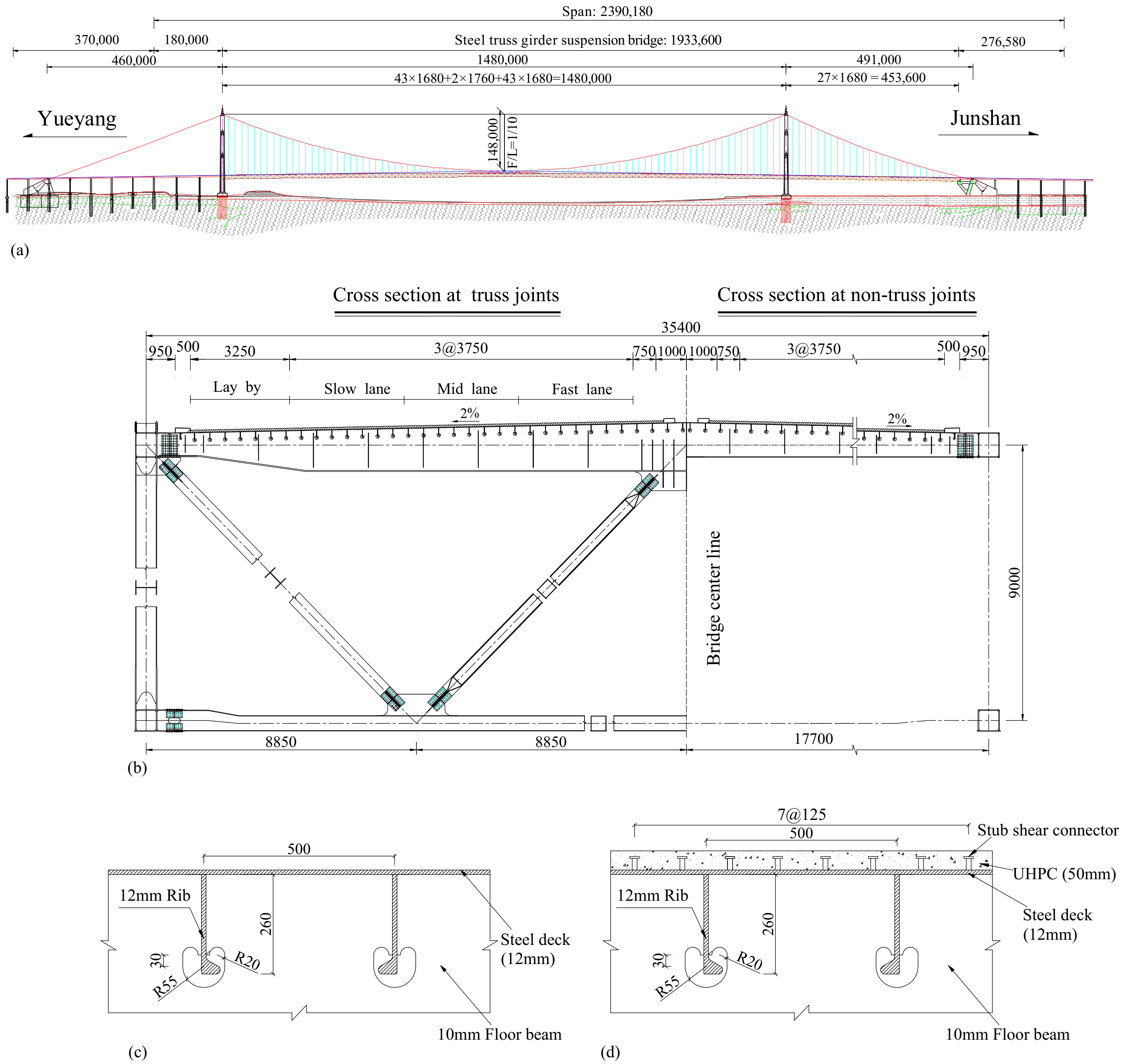

Fig. 1. Schematic diagrams of the SDTL Bridge (all dimensions are in millimeters): (a) elevation view; (b) cross section of the steel truss girder; (c) local view of a conventional OSD; (d) the proposed LWCD scheme

The stress-evaluation methods and the fatigue strengths of six details (Fig. 2) are given in Table 1, in which the fatigue strengths were determined on the basis of Eurocode 3 (ECS 2005).

Finite-Element Models

It is preferable to use solid elements to build finite-element models. However, the computing cost would increase significantly if the whole deck system were simulated by solid elements. Consequently, the authors used the submodel technology to save computing effort. Thus, the finite-element models were built at two levels through *ANSYS 14.0* software.

In the first level, a deck segment of the SDTL Bridge was created. This finite-element model is referred to as FE Model 1 (shown in Fig. 4). Considering the symmetry of the deck, only half of the deck was modeled. As mentioned earlier, both the conventional OSD scheme and the LWCD scheme were considered in the analysis. The conventional OSD finite-element model contained only steel components that were built by using the 8-node shell elements (SHELL91). The elastic modulus and Poisson's ratio of the steel were defined as 206 GPa and 0.3, respectively (ECS 2004). Although for the finite-element model of the LWCD, the OSD was modeled by the SHELL91 elements, the UHPC layer was modeled by the 20-node solid elements (SOLID95), and the stud shear connectors were modeled by the 2-node spring elements (COMBINE14). The shear stiffness of the stud

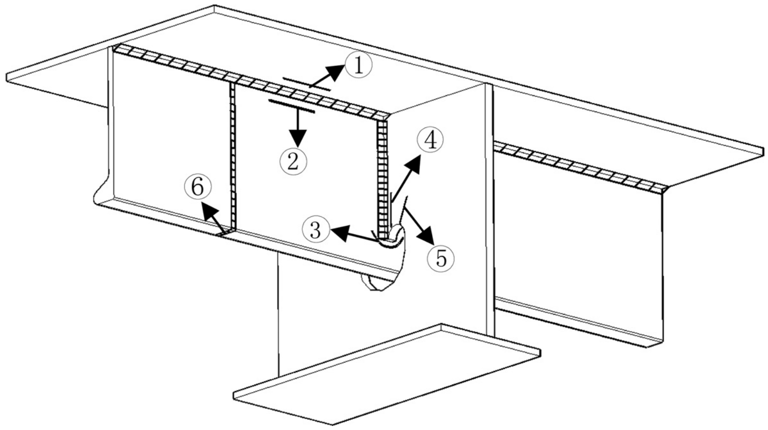

Fig. 2. Typical fatigue-prone details of an OSD with open ribs

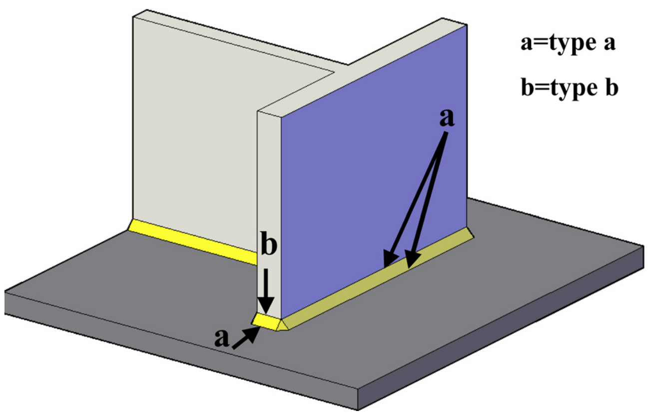

Fig. 3. Types of hot spots

Table 1. Fatigue Strength of Typical Fatigue-Prone Details in OSDs

Detail(s)	FAT (2×10^6 cycles) (MPa)	CAFL (1×10^7 cycles) (MPa)	VAFCL (1×10^8 cycles) (MPa)	Stress type
1–4	90	52.6	33.2	Hot spot
5	125	73.0	46.0	Nominal
6	90	52.6	33.2	Nominal

Note: CAFL = constant-amplitude fatigue limit; FAT = fatigue class; VAFCL = variable-amplitude fatigue cutoff limit.

shear connectors was defined as 120 kN/mm, which was derived from the results of push-out tests for stud shear connectors embedded in UHPC (Li et al. 2015).

The FEA in this paper did not account for the material nonlinearity of the UHPC, and the reasons are as follows. On the one hand, experimental investigations by Shao et al. (2013) revealed that the reinforced UHPC exhibited high cracking strength (i.e., 42.7 MPa). On the other hand, their theoretical analyses indicated that the maximum tensile stress of the UHPC layer was only 10.08 MPa under design traffic loads, much less than its cracking strength. Thus, the UHPC layer is assumed to behave in the linear-elastic range. The elastic modulus and Poisson's ratio of UHPC were 42.6 GPa and 0.2, respectively (Shao et al. 2013).

In FE Model 1, the regions of interest were finely meshed, and the element grid size was set to 4.8 mm, whereas the remaining parts of the model were coarsely meshed. For simplicity, the bulb flat ribs were assumed to be angle ribs that possessed identical moments of inertia and areas.

The boundary conditions of FE Model 1 were as follows: (1) nodes in the two end floor beams were restricted from translations in the *y*-direction (vertical translations) and from rotations relative to the *x*- and *y*-axes; (2) nodes on the transversal symmetry plane were constrained with symmetric constraints about the *y*–*z* plane; and (3) nodes at the end of the web in the floor beams where vertical suspenders existed were restricted from translations in the *y*-direction (vertical translations).

On the second level, solid submodels (FE Model 2) were built on the basis of FE Model 1 (shown in Fig. 5). FE Model 2 was built using the 20-node solid elements (SOLID95), which simulated a local region containing the rib–floor beam joint. Fillet welds were assumed to have triangular profiles (Liu et al. 2014) in FE Model 2. The minimum mesh grid size in the region of interest was 2 mm.

Node that displacements in FE Model 1 were obtained and exerted on corresponding nodes at the edge of FE Model 2. By doing so, the boundary condition of FE Model 2 was defined, and the model could reflect its local behaviors.

For Detail 4 in FE Model 2, the hot spot stresses were captured on the basis of quadratic extrapolations along a curved path (Fig. 5). According to studies by Aygül et al. (2012), this method is suitable for the rib–floor beam welds, for which a straight extrapolation path does not apply.

Loads

Fatigue cracks in OSDs are usually caused by local loads. For this paper, Fatigue-Load Model 3 in Eurocode 1 (ECS 2003) was selected for the analyses. According to Eurocode 1 (ECS 2003), the fatigue-load model is a single-vehicle model that consists of four axles. The weight of each axle is 120 kN, and the contact area of each wheel is a square with a side length of 0.4 m.

According to investigations by Xiao et al. (2008), a wheel generates significant stresses to only a local region of the deck underneath the wheel. Thus, OSDs respond in a very localized way when exposed to traffic loads, and only the two rear axles, spaced 1.2 m from each other (120 + 120 kN), were taken into account in the analysis for simplicity, which implies that the other group of axles was ignored due to their limited influences.

In the analysis, three transversal loading cases were considered [Fig. 6(a)]. For each load case, the fatigue load was put on different

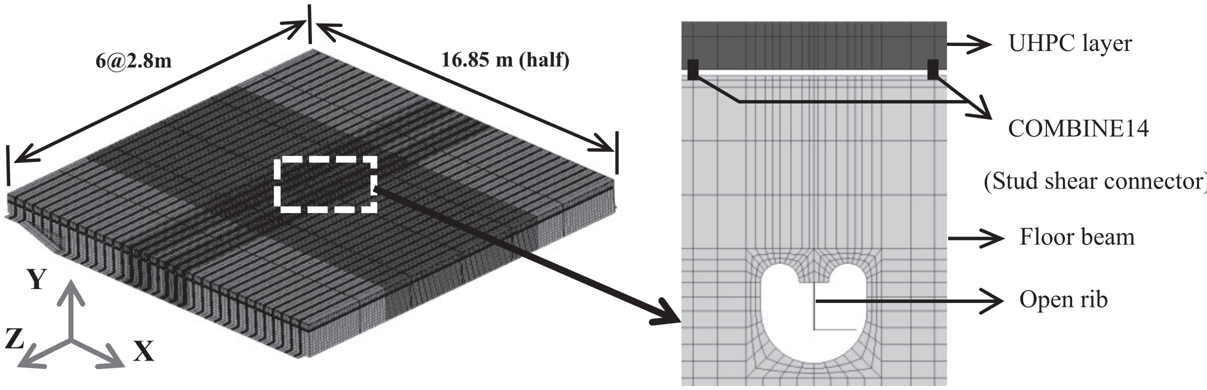

Fig. 4. FE Model 1

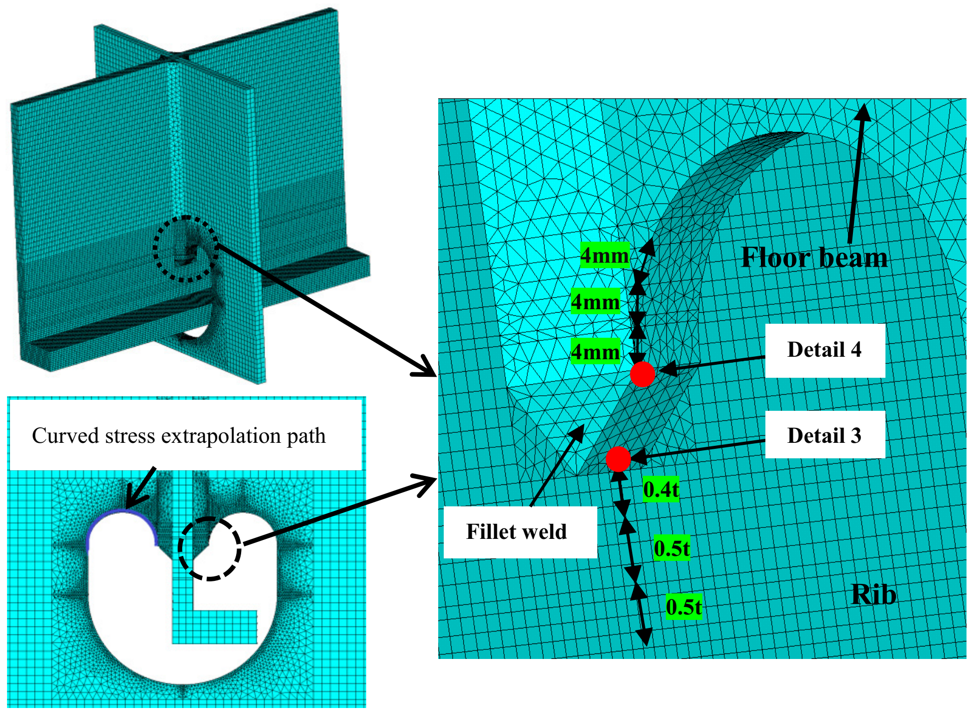

Fig. 5. FE Model 2 (submodel)

longitudinal positions (z-axle) to simulate the running of the vehicle.

The stress ranges in the OSD were checked at 11 sections, as shown in Fig. 6(b). For Details 1 and 2 (the rib–deck welded joints), the stress ranges were investigated at Sections 1–9. For Detail 6 (the splice weld in open ribs), the stress ranges were checked at Sections 10 and 11. For Details 3–5, located at the rib–floor beam sections, the stress ranges were captured at Floor Beams (FBs) 3, 4, and 5.

Calculation Results and Discussion

The stress histories for each fatigue detail were obtained by checking all of the load cases and the related sections of interest. The stress ranges of the six fatigue details were then determined via the reservoir method, and the maximum stress ranges are listed in Table 2. It should be noted that the stresses in Details 1, 2, and 6 were obtained from FE Model 1, and the stresses in Details 3–5 were captured from FE Model 2.

According to the data in Table 2, the following was easily observed: (1) attributable to the contribution of the UHPC layer, the stress ranges of six fatigue details were reduced by 35.1–87.3% for the open-ribbed OSD; (2) in the LWCD, the stress ranges of Details 1, 2, and 6 were less than their CAFLs, and as a consequence, these three details are expected to have theoretically infinite fatigue life cycles; and (3) although they had decreasing amplitudes of 49.4–69.6%, the stress ranges of Details 3 and 5 in the LWCD were still high. In particular, the stress range of Detail 5 was above its CAFL (i.e., 73.0 MPa).

The preliminary FEA indicated that extra attention should be paid to Details 3 and 5 for the LWCD because they had relatively high stress ranges. Thus, these two details should be adequately designed to prevent fatigue cracking in service. As a consequence, further analyses were performed to reveal the behaviors of these details, which are presented in the next section.

The FEA also revealed that the shear studs had a maximum shear stress range (i.e., $\Delta\sigma = \sigma_{\max}–\sigma_{\min}$) of 48.8 MPa. According to

J. Bridge Eng., 2016, 21(7): 04016039

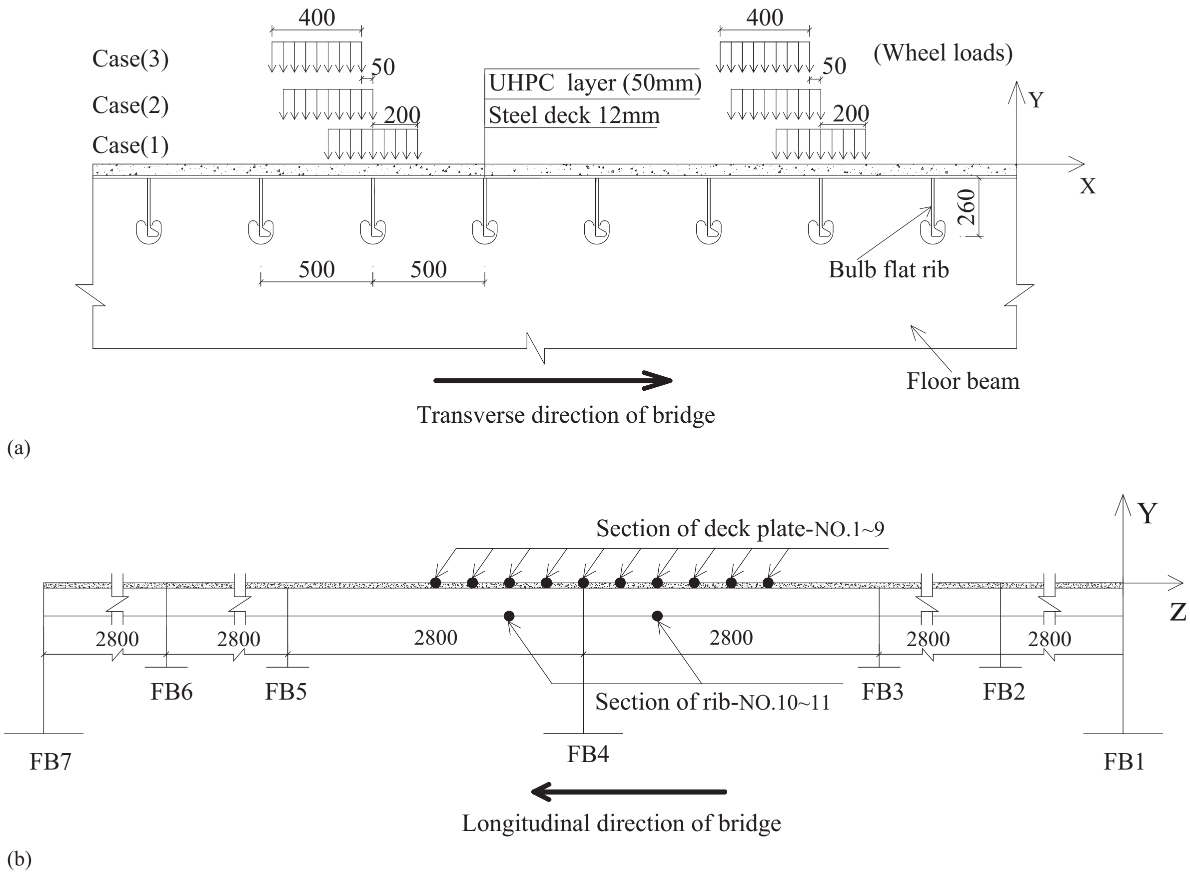

Fig. 6. Schematic diagrams for load cases and sections of interest (all dimensions are in millimeters): (a) load cases in transversal direction; (b) sections of interest (Note: FB = Floor beam; UHPC = ultrahigh-performance concrete)

Table 2. Maximum Stress Ranges of Fatigue-Prone Details

Position	Detail	Type of hot spot	Stress direction	Stress range (MPa)		CAFL (MPa)	Amplitude reduction (%)
				OROSD	LWCD		
Rib–deck	1	a	SX	199.9	27.8	52.6	86.1
	2	a	SY	104.2	13.2	52.6	87.3
Rib–floor beam	3	a	SY	161.6	49.0	52.6	69.6
	4	b	S1	17.2	8.7	52.6	49.4
	5	—	S1	195.4	98.0	73.0	49.8
Butt weld of ribs	6	—	SZ	74.7	49.3	52.6	33.6

Note: In calculation of the amplitude reduction, the stress ranges in the OROSD are referred to as the bases. CAFL = constant-amplitude fatigue limit; LWCD = lightweight composite deck; OROSD = open-ribbed orthotropic steel deck; S1 = principle stress.

Eurocode 3 (ECS 2005), the fatigue strength of welded studs at 2 million cycles is 90 MPa. Thus, the studs in the LWCD should be able to safely resist cyclic traffic loads. In addition, results of the FEA indicated that the deck plate at the stud–deck interconnections had a maximum stress range of 14.0 MPa. In Eurocode 3 (ECS 2005), such fatigue-prone detail has a fatigue strength of 80 MPa (at 2 million cycles). It is clear that the deck plate should also be safe when exposed to cyclic traffic loads.

Parametric Studies

For this section, parametric studies were conducted for the LWCD to explore the influence of different parameters on the fatigue behavior of Details 3–5. Two parameters were considered: (1) the shape of cutouts on the web of the floor beams and (2) the thickness of the floor beams. The method used to establish finite-element models was identical to that described in the previous section.

Parameter 1: Shape of Cutouts

The shape of cutouts on the floor beams plays an important role in fatigue responses of the rib–floor beam connections. Four types of cutouts were selected and compared in the analyses (Fig. 7). Other parameters of the LWCD were identical to those shown in Fig. 1.

Four groups of finite-element models were built on the basis of four cutout schemes. Each group consisted of two finite-element models, namely, a deck segment finite-element model of the LWCD and a solid submodel. The hot spot stresses were captured on the basis

J. Bridge Eng., 2016, 21(7): 04016039

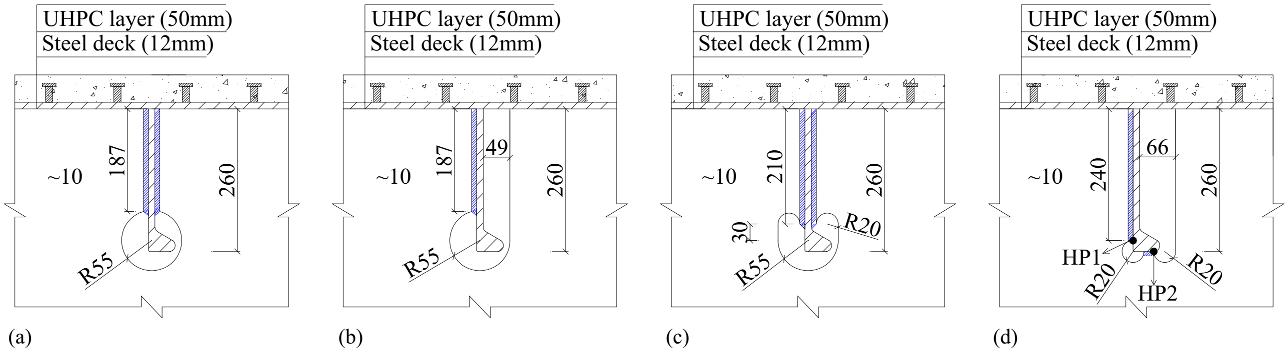

Fig. 7. Four cutout schemes (all dimensions are in millimeters): (a) Cutout 1; (b) Cutout 2; (c) Cutout 3; (d) Cutout 4 (Note: UHPC = ultrahigh-performance concrete)

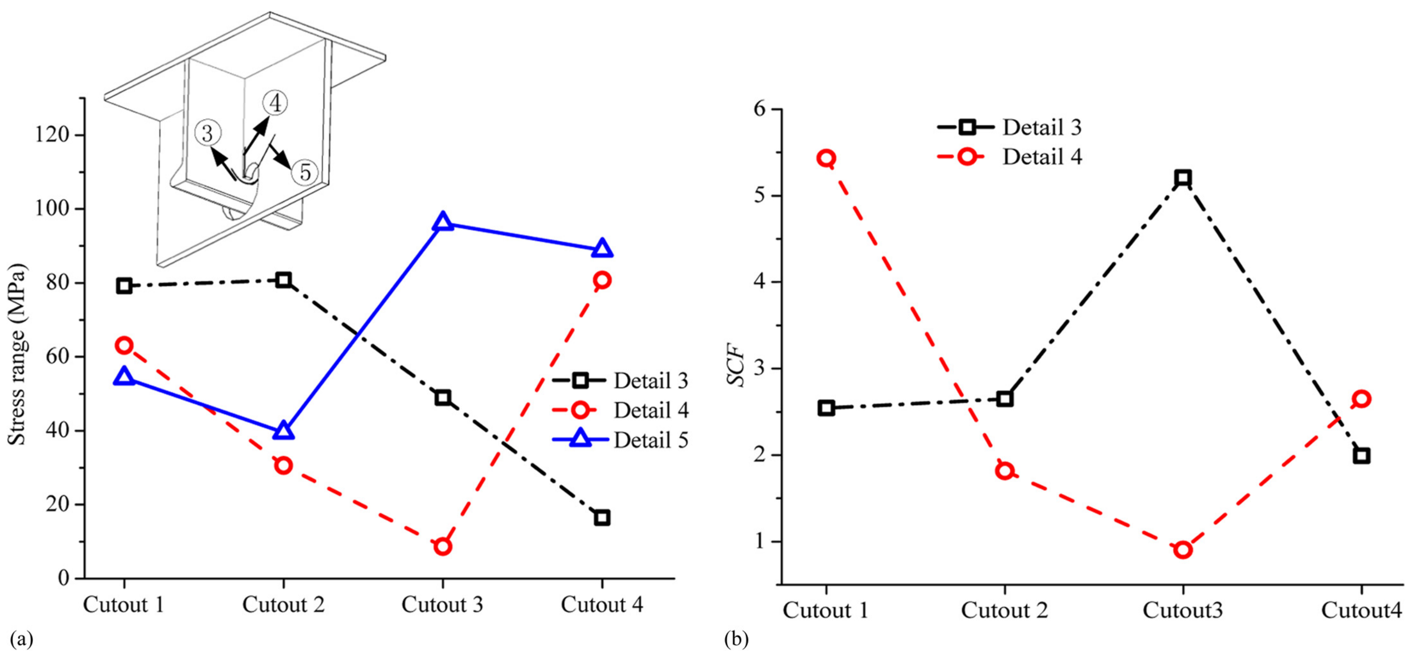

Fig. 8. Calculation results of Parameter 1 analysis: (a) stress ranges of three fatigue details; (b) stress concentration factors of Fatigue Details 3 and 4

of a method identical to that described in the section titled "FEA." It should be noted that straight stress extrapolation paths were used for all of the cutout schemes except for Cutout 3. For Cutout 3, a curved stress extrapolation path (Fig. 5) was used, because the space in the floor beam near the weld tip was too narrow.

Fatigue cracking is generally accompanied by stress concentrations. The stress concentration factor (SCF) is typically used to evaluate the extent of the stress concentration phenomenon. The SCF is defined as the ratio of the hot spot stress to the nominal stress for a given fatigue detail, i.e., SCF $= \sigma_{\text{hot}}/\sigma_{\text{nom}}$, where σ_{hot} = hot spot stress; and σ_{nom} = nominal stress. Here, the nominal stress is defined as stress obtained at a point 1.5t (where t is the thickness of the steel plate) from the weld toes (Hobbacher 2008).

The hot spot stresses and the SCFs for the details of interest (i.e., Details 3–5) were obtained from the submodels, and the results are shown in Fig. 8.

Fig. 8 indicates that, in terms of the fatigue behaviors of Detail 3, Cutout 4 is the most favorable among the four. Cutout 4 has the lowest stress range and SCF, which might be attributable to the fact that the bottom of the bulb flat ribs was welded to the web of the floor beams in Cutout 4, which effectively constrained the deformation of the ribs. As a consequence, the hot spot stress and the SCF of Detail 3 [Fig. 7(d), HP1] were less prominent. A cutout similar to Cutout 4, with the bottom of the U-shaped ribs welded to the floor beams, was analyzed by Tang et al. (2014). However, Tang et al (2014) concluded from their observations that HP2 [Fig. 7(d)] was more susceptible to fatigue cracks than HP1 [Fig. 7(d)] because the hot spot stress at HP2 was much higher. Although the SCF of Cutout 3 was the highest among the four, its stress range was much lower than those in Cutouts 1 and 2.

For Detail 4, both the hot spot stress and the SCF of Cutout 3 were the minimum. Cutout 3 has significant advantages over other cutouts, because the special rib–floor beam joints in Cutout 3 could release the local deformation of the ribs. It was also observed that Cutout 1 had the maximum SCF, which indicates that Cutout 1 is prone to fatigue cracking at Fatigue Detail 4, which has been confirmed by experimental investigations (Aygül et al. 2012).

For Detail 5, the stress ranges of Cutouts 3 and 4 maintained high levels because a small radius (20 mm) was adopted. Thus, Detail 5 in Cutout 3 was vulnerable to fatigue cracks, which is unfavorable.

Research by Frýba and Gajdos (1999) indicated that the radii of cutouts should be neither too small, which can lead to severe stress concentrations, nor too large, which might weaken the floor beams by reducing the cross-sectional area. Thus, Frýba and Gajdos (1999) recommended that the radii of the cutouts be 40–50 mm.

To summarize, there was no cutout scheme that outperformed the others in both stress range and SCF when all three fatigue details were considered. Both the hot spot stress and the SCF of Cutout 4 maintained a high level at HP2 (Fig. 7) and might lead to fatigue cracking. This result was confirmed by the HaiMen Bridge, a steel bridge in China in which a cutout similar to Cutout 4 was used (Fig. 9) and in which multiple fatigue cracks initiated and propagated at HP2 (Zhang 2011). Thus, Cutout 4 is not recommended for highway bridges. Cutout 2, which also exhibited poor fatigue properties because of its asymmetrical geometry (Frýba and Gajdos 1999), is also not recommended. It is apparent that stress ranges of Details 3 and 4 in Cutout 1 were higher than that the stress ranges in Cutout 3. As a consequence, Cutout 3 is recommended for the SDTL Bridge.

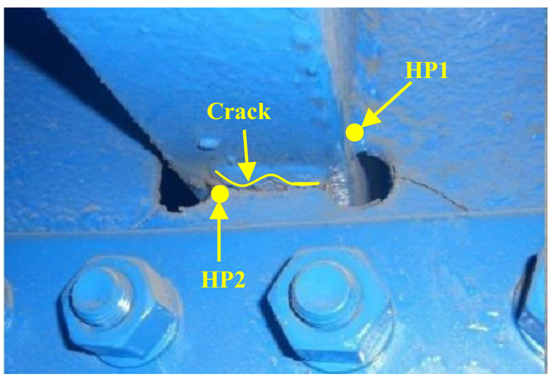

Fig. 9. Fatigue cracks at the rib–floor beam joints in the HaiMen Bridge (Zhang 2011) (Note: HP1 = Hot Spot Point 1; HP2 = Hot Spot Point 2)

Parameter 2: Thickness of Floor Beams

In this subsection, further parametric studies were conducted for the recommended Cutout scheme only, i.e., Cutout 3. In the analysis, the thickness of the floor beams ranged from 8 to 18 mm with increments of 2 mm. Six groups of finite-element models were established correspondingly. Other parameters were identical to those described in the section titled "Brief Introduction to the Second Dongting Lake Bridge."

The calculation results are shown in Figs. 10 and 11. Fig. 10 illustrates the stresses and the SCFs of the three fatigue details, and Fig. 11 presents the in-plane and out-of-plane stress components of Detail 5 in the floor beams.

Fig. 10(a) shows that the stress range of Detail 5 decreased significantly with the increasing thickness of the floor beams, whereas the thickness increase had limited influences on Details 3 and 4 in that the hot spot stress ranges of Details 3 and 4 both had only slight changes.

Fig. 10(b) shows that the SCF of Detail 3 was reduced with the increasing thickness of the floor beams. The reason might be that a thicker floor beam results in a larger profile dimension in the rib–floor beam welds, leading to a more uniform stress distribution in front of the weld tips. Although the SCF of Detail 4 exhibited an increasing trend with the increasing thickness of the floor beams, the values were, in general, approximately 1.0.

Fig. 11 shows that in Detail 5, the in-plane stress component was much higher than the out-of-plane stress component. With the thickness of the floor beams increased, the in-plane stress decreased significantly, whereas the out-of-plane stress remained nearly unchanged.

In summary, it is generally favorable to increase the thickness of the floor beam in terms of fatigue stresses in Details 4 and 5. In addition, although it is somewhat unfavorable to increase the thickness of the floor beams for Detail 3, which resulted in a slight increase in stress ranges, the stress range of Detail 3 was below its CAFL when the thickness did not exceed 18 mm. It is apparent in Fig. 10(a) that the stress ranges of the three fatigue details were all lower than their

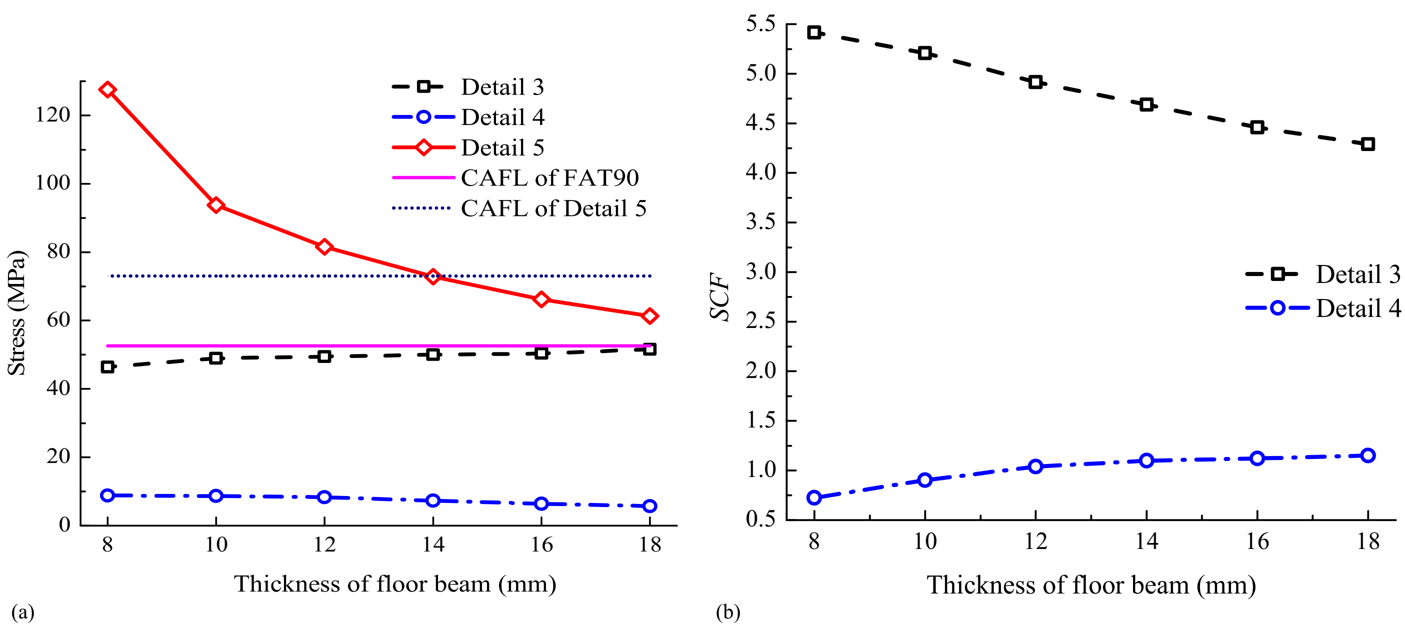

Fig. 10. Stress ranges and concentration factors versus thickness of floor beams: (a) stress ranges; (b) stress concentration factors (Note: CAFL = constant-amplitude fatigue limit; FAT = fatigue class)

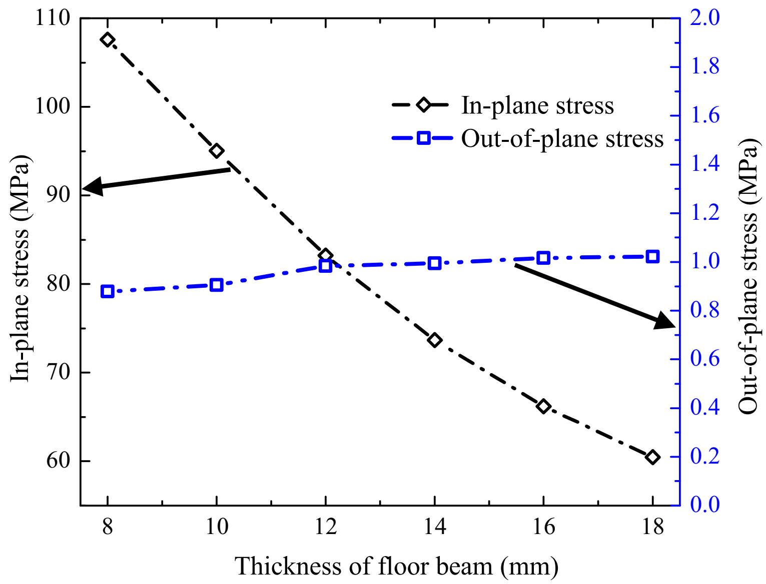

Fig. 11. In-plane and out-of-plane stress components in Detail 5 with changing thickness of the floor beams

corresponding CAFLs when the thickness of the floor beams is between 14 and 18 mm.

Thus, on the basis of the previous analysis and discussion, a 16-mm-thick floor beam with apple-shaped cutouts is recommended for the open-ribbed LWCD of the SDTL Bridge.

Fatigue Tests

This section presents two fatigue tests. The aim of the tests was to reveal the fatigue endurance of the OSD and the stud shear connectors.

Fatigue Test 1: Composite Deck Panel

Test Setup and Loading Scheme

A full-scale specimen with dimensions of 5,200 mm (length) × 3,500 mm (width) × 1,062 mm (height) was manufactured (Fig. 12). This LWCD segment consisted of an OSD panel and a 50-mm UHPC layer. The OSD consisted of a 12-mm deck plate, seven longitudinal bulb flat ribs, and two 16-mm-thick transverse floor beams. The type of the bulb flat ribs was HP260, which has a height of 260 mm and a thickness of 12 mm. The steel material of these components was Q345qD, a steel grade for bridges in China that has a yield strength of 345 MPa. The UHPC layer was reinforced by steel meshes, spaced 37.5 mm in both the longitudinal and transverse directions. At the OSD–UHPC interface, stud shear connectors (spaced 125 mm apart) were applied to provide a robust connection. All of the materials and manufacturing procedures were the same as those to be applied to the SDTL Bridge.

As shown in Fig. 12, the full-scale specimen was placed on four supports located below the flange of the floor beams. The load was applied to the top center of the UHPC layer at the cantilever region through a hydraulic jack. The load had a print area of 200 mm (length) × 600 mm (width). The specimen was loaded at a CAFL with $p_{max} = 200.0$ kN and $p_{min} = 20.0$ kN. The load frequency was 3.0 Hz.

It is apparent in Fig. 12 that Section A–A had the maximum stress responses and Section B–B had the maximum deflections. Thus, strain gauges were attached to fatigue-prone details of interest at Section A–A, including Details 3 and 5. Approximately 110 strain gauges were mounted to the free edge of the apple-shaped cutouts, because this fatigue detail is unfavorable. Two dial indicators were attached to the bottom of the ribs at Section B–B to observe the deflections. In addition, eight dial indicators were placed on the supports to record possible tiny, rigid body displacements of the whole specimen. Fig. 13 shows photographs of the fatigue test.

Determination of Stress Ranges

Before the fatigue test, a series of static tests was performed for the specimen to determine its stresses under the maximum and minimum loads and thus to determine the stress ranges (Ouyang et al. 2014). Meanwhile, a finite-element model was built for the full-scale specimen. The method of establishing the finite-element model was identical to that described in the section titled "FEA."

The static test revealed that the stress ranges of Fatigue Details 5 and 3 were 90.6 MPa (95.8 MPa) and 50.5 MPa (55.3 MPa), respectively (the values in parentheses were obtained from the FEA). It can be seen that the tested data agree well with the FEA results, which reflects the accuracy of the FEA in this paper. For Fatigue Detail 4, the stress range was not recorded in the static tests because this detail had a curved shape, which made it difficult to install the strain gauges. Thus, the stress range obtained from the FEA was used for this detail (i.e., 8.1 MPa). It was apparent that Fatigue Detail 5 was the most unfavorable one among the three in the fatigue test.

To record the strains and deflections of the specimen after experiencing certain cycles of loading, the fatigue load was suspended for a while, and static tests were then carried out.

Results of Fatigue Test 1

After being loaded by 2.5 million cycles, the specimen remained intact with no cracks observed in any of the fatigue details. The fatigue test was then terminated. Recorded data from the measurement points indicated that the stresses and deflections of the specimen had only slight changes after such a large number of load cycles. The test results are plotted in Fig. 14. In addition, the UHPC layer also developed no fatigue cracks.

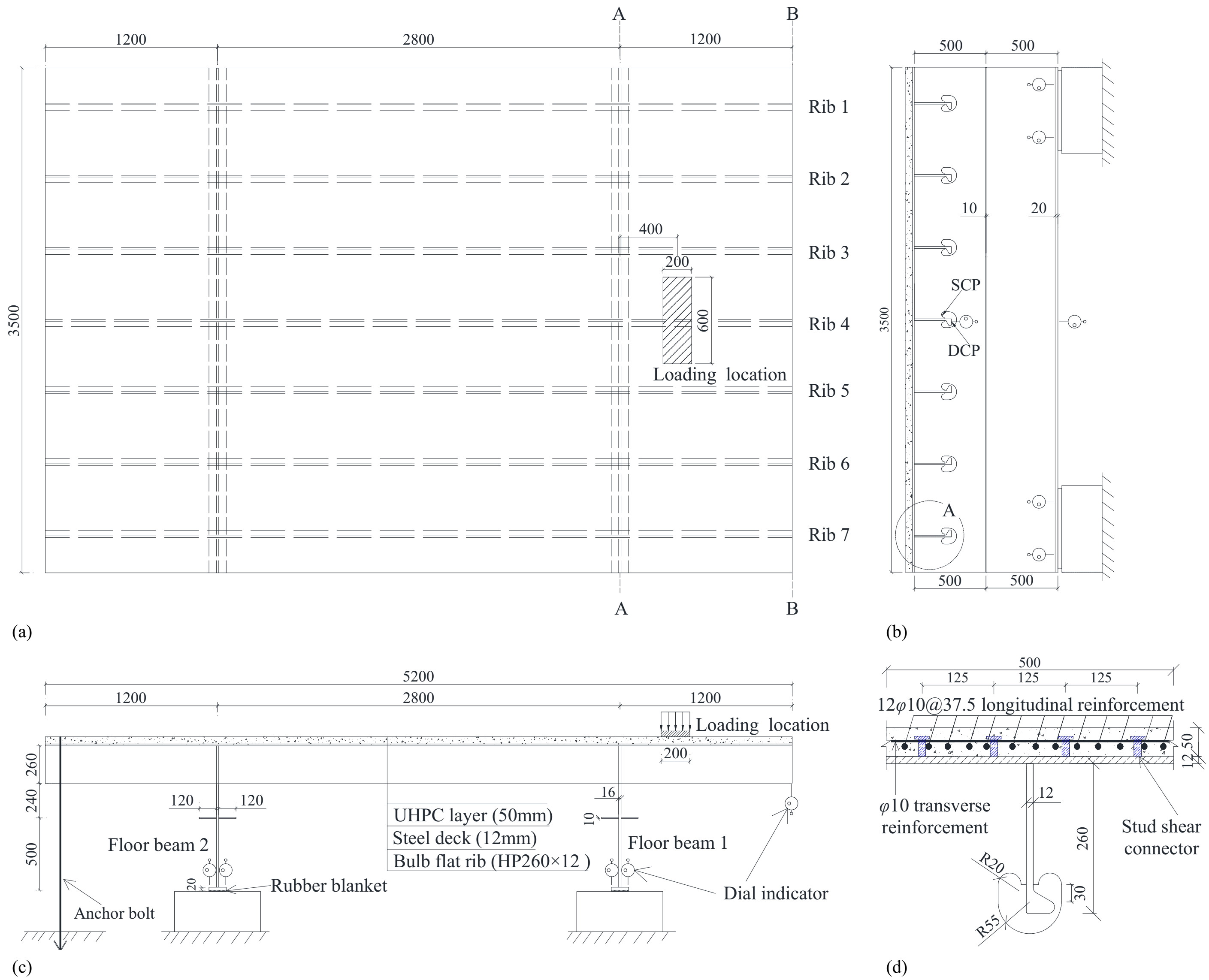

Fig. 12. Setup of the full-scale specimen for Fatigue Test 1 (all dimensions are in millimeters): (a) planner view; (b) cross-sectional view; (c) elevation view; (d) details of A [circled section in (b)] (Note: DCP = displacement control point; SCP = stress control point; UHPC = ultrahigh-performance concrete)

Fig. 14(a) indicates that the strains at Fatigue Detail 5 increased approximately linearly with the ascending static loads, which means that Detail 5 exhibited no obvious fatigue damage after experiencing fatigue loadings up to 2.5 million cycles. In addition, there were only small differences between the peak strains under different cycles.

Fig. 14(b) shows that the deflection of the specimen at Section B–B also increased approximately linearly with the increasing static loads. The load–deflection curves obtained at different load cycles were quite close to each other. These observations indicate that there was no obvious stiffness reduction in the specimen.

According to the Palmgren–Miner linear cumulative rule, different stress ranges satisfy the relationship as follows:

$$N' = \sum_{i=1}^{n} \left(\frac{\sigma_i}{\sigma'}\right)^m n_i \tag{1}$$

where σ' = design stress range (in MPa); σ_i = random stress range (in MPa); m = slope of the S–N curve, the value of which is 3.0; n_i = loading cycles for the ith random load; and N' = equivalent loading cycles of the design load.

For the fatigue test, the design stress range is $\sigma' = 66.2$ MPa [Fig. 10(a)]; the random load refers to the load in the fatigue test, i.e., $i = 1$, and $\sigma_i = 90.6$ MPa. Substituting these values into Eq. (1), it is found that $N' = 6.4 \times 10^6$, which implies that the conducted fatigue test is equal to 6.4 million cycles of loading for Detail 5 at its design stress range.

The fatigue test is further discussed here. It is known that OSD bridges might suffer from more than 100 million cycles of vehicle loading during their service life. However, the level of stresses induced by most vehicles is below the fatigue stress limit and will not contribute to the fatigue damage of OSDs. Practice has shown that the majority of vehicle-induced stress cycles are below the fatigue limit and therefore can be neglected (Chen et al. 2014), which implies that only a small portion of vehicle-induced stress cycles needs to be considered in fatigue verification.

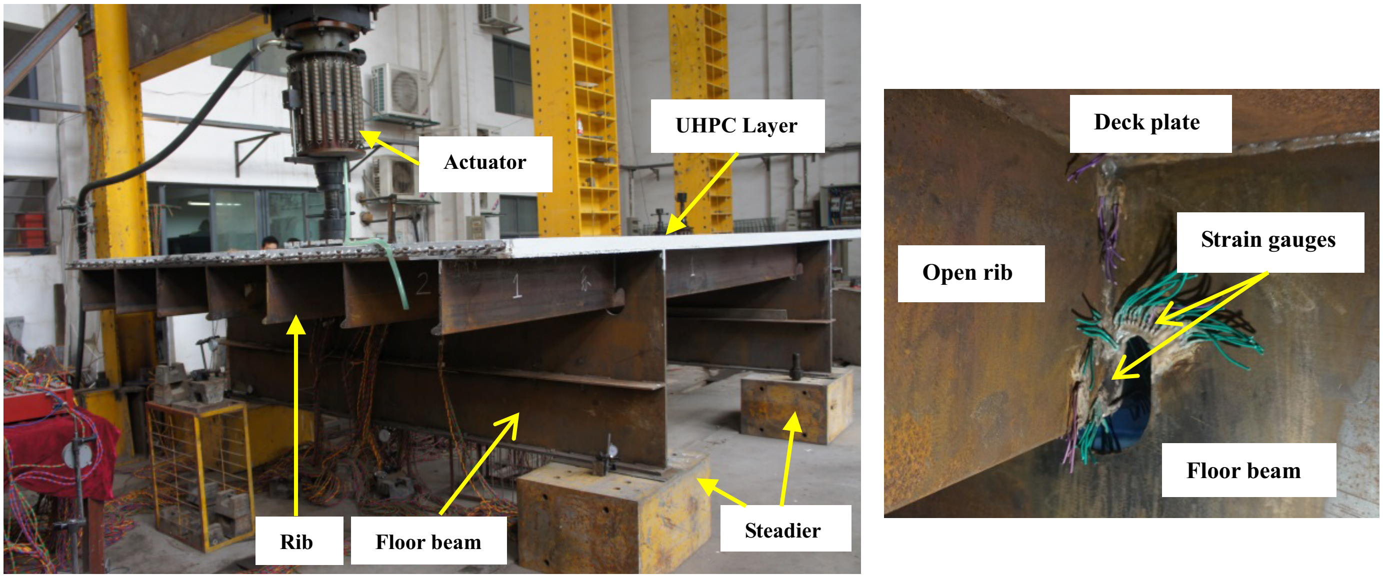

Fig. 13. Photos taken from Fatigue Test 1 (Note: UHPC = ultrahigh-performance concrete)

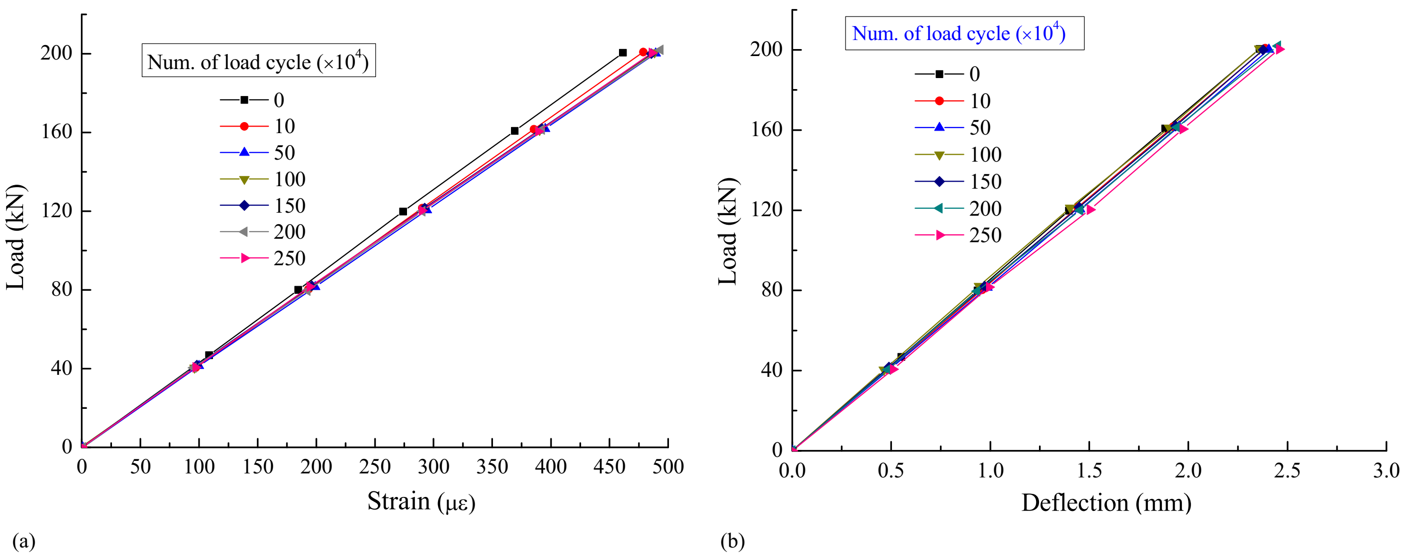

Fig. 14. Test results: (a) load–strains of Detail 5; (b) load–deflection curves of Section B–B

Thus, for fatigue test here, the authors followed the design philosophy in Eurocode 3. Eurocode 3 requires steel bridges (including OSD bridges) to have a fatigue life of no less than 2 million cycles. As mentioned already, the equivalent loading cycle for the fatigue-prone detail under the design loads was estimated to be 6.4 million cycles, a value that exceeds 2 million. Thus, the test revealed that the detail can meet the design requirement of Eurocode 3 in terms of fatigue.

Fatigue Test 2: Strip Specimen Test for Stud Shear Connectors

Test Setup and Loading Scheme

The test here was aimed at revealing the fatigue characteristic of stud shear connectors embedded in UHPC and to validate the feasibility of applying stud shear connectors to the SDTL Bridge. The test was based on an OSD–UHPC composite beam specimen simulating a strip of the SDTL Bridge. The specimen was 3,200-mm long and 1,000-mm wide (Fig. 15), and it consisted of two longitudinal open ribs.

The stud shear connectors had a diameter of 13 mm and a height of 35 mm and were spaced 125 × 125 mm (longitudinal × transversal). Before casting the UHPC layer, an organic silicon release agent was brushed on the steel deck of the specimen to eliminate bonding and friction at the interface. As a result, the test results should be conservative, because such bonding and friction exist in actual bridges, which provides extra connections at the interface.

The load was exerted to the specimen from the top center at Section A–A [Fig. 15(a)], which resulted in positive bending moment in the specimen between the two supports. The fatigue test consisted of two steps. A FEA based on the two load steps was performed for the specimen. The calculation results reveal that, in the first load step, the maximum nominal shear stress range of the stud

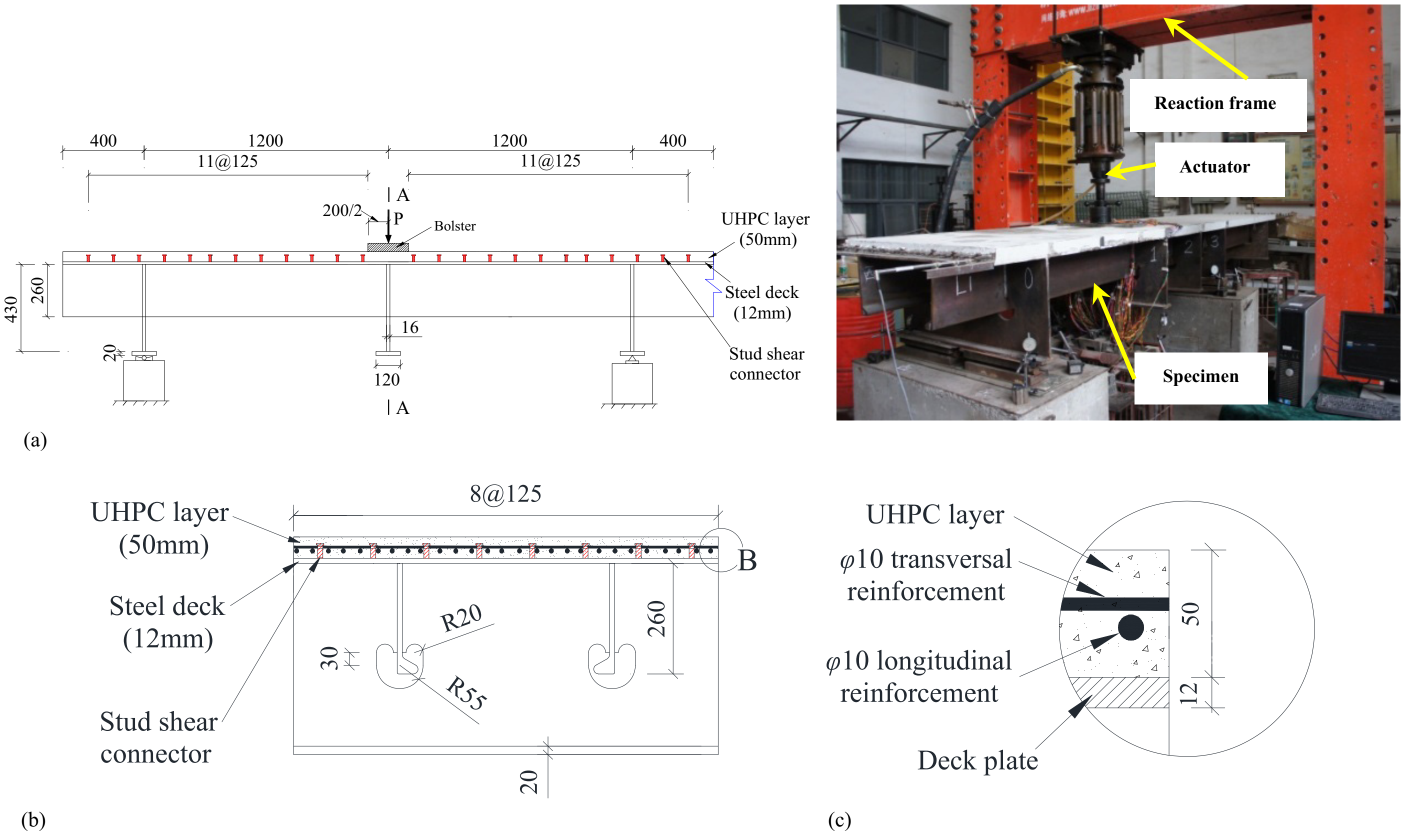

Fig. 15. Setup and loading scheme for Fatigue Test 2 (all dimensions are in millimeters): (a) elevation view and photograph of the test; (b) cross-sectional view; (c) Detail B (Note: UHPC = ultrahigh-performance concrete)

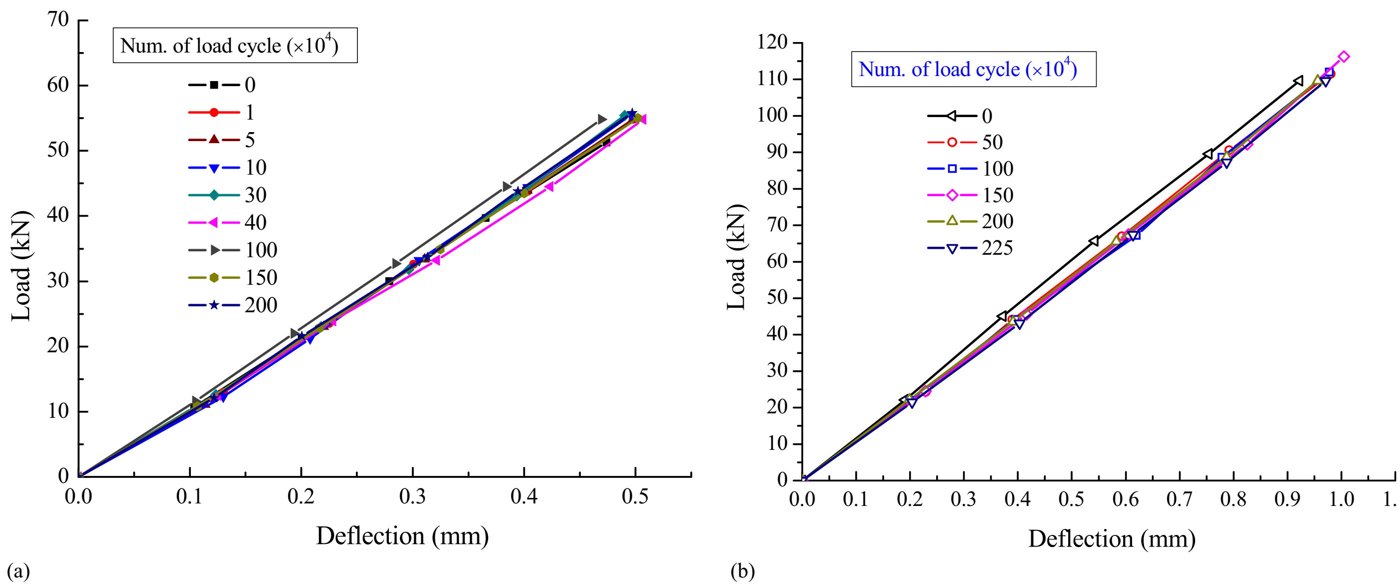

Fig. 16. Load–deflection curves: (a) first fatigue load step; (b) second fatigue load step

shear connectors was 35.5 MPa, whereas in the second load step, the maximum nominal shear stress range was 77.4 MPa. The cycles of the first and the second load steps were 2.0 and 2.25 million, respectively. The frequency of both fatigue loads was 4.0 Hz.

Dial indicators were mounted to the specimen at Section A–A and at the support positions. After certain cycles of loading, the fatigue test was suspended for a period, and static tests were performed instead to record the deflection data.

Test Results and Discussion

Through the two steps of the fatigue test, no slip cracks were observed at the OSD–UHPC interface. When the accumulative loading cycles reached certain numbers, the fatigue load was suspended for a period, and a static load test was performed instead. The load–deflection relationships of the specimen after experiencing certain cycles of loading are shown in Fig. 16.

In Fig. 16, the load–deflection curves obtained at different loading cycles exhibited only little differences, which implies that the stiffness of the specimen barely reduced during the fatigue test, indicating that the specimen was in a good state after experiencing the fatigue loading.

To evaluate the fatigue safety of stud shear connectors to be used in the SDTL Bridge, the design shear stress range of studs in the LWCD of the SDTL Bridge was obtained from the FEA described in the section titled "Parametric Studies." The FEA results revealed that the stud shear connectors had a maximum stress range of 48.8 MPa under the design loads.

According to the Palmgren–Miner linear cumulative rule, different stress ranges satisfy Eq. (1), as described in the subsection titled "Fatigue Test 1: Composite Deck Panel." The only difference is the slope of the *S–N* curve *m*; for studs, $m = 8.0$. Two kinds of constant-amplitude loads were adopted in the fatigue test in this section, i.e., $n = 2$: $\sigma_1 = 35.5$ MPa, $n_1 = 2 \times 10^6$ and $\sigma_2 = 77.4$ MPa, and $n_2 = 2.25 \times 10^6$. In addition, the maximum design shear stress range for the studs is $\sigma' = 48.8$ MPa. Substituting these values into the equation, it is found that $N' = 9.0 \times 10^7$, a value much greater than 2 million. As a consequence, it can be predicted that the stud shear connectors will meet the fatigue design requirements of the SDTL Bridge.

Behavior of UHPC in LWCD

Static Test for LWCD under Negative Bending Moment

After Fatigue Test 2, a static load test was performed on the composite beam specimen. The aim of the static test was to observe the behavior of the composite beam under negative bending moments and to justify the feasibility of the linear elastic assumption for the UHPC in FEA (as presented in the section titled "FEA"). The loading scheme and photographs for the static test are shown in Fig. 17. It can be seen that the most unfavorable Section is B–B.

The UHPC investigated in this paper was specially developed for OSDs by the research group at Hunan University in Changsha, China. A detailed list of the materials is presented in Table 3. It should be noted that two types of steel fibers were used for the UHPC, and both types of them have a tensile strength of ≥2,800 MPa. The UHPC has a cubic compressive strength of 155.2 MPa, a flexural strength of 29.9 MPa, and an elastic modulus of 42.6 GPa.

Considering that both the specimen and the load were symmetric, only the left half of the specimen (Fig. 17) was selected to explain the test results. When the loading reached 166.5 kN, the maximum tensile strain of the UHPC layer was 1,236 $\mu\varepsilon$, but there were no visible cracks on the surface of the UHPC layer. When the load was further increased to 179.0 kN, the first visible crack appeared on the top of the UHPC layer at Section B–B. At the onset of cracking, the maximum crack width was 0.05 mm, and the maximum strain of the UHPC was 1,444 $\mu\varepsilon$. When the load reached 216 kN, the maximum crack width became 0.1 mm.

To verify the test results, two FE models were established. One was built by considering only the elastic linear behavior of UHPC, and the other took into account the nonlinear properties of UHPC. The linear FE model was built through *ANSYS* software, following methods identical to those described previously. The nonlinear finite-element model was established using *Abaqus 6.14* software,

Table 3. Ingredients of Ultrahigh-Performance Concrete

Item	Ingredient	Value
Weight (kg/m^3)	Cement	771.2
	Silica fume	154.2
	Fly ash	77.1
	Quartz sand	848.4
	Quartz powder	154.2
	Superplasticizer	20.1
	Water	180.5
	Steel fibers	
	Type 1	118
	Type 2	157
Weight ratio	Cement	1.0
	Silica fume	0.2
	Fly ash	0.1
	Quartz sand	1.1
	Quartz powder	0.2
	S/P ratio (%)	2
	W/P ratio	0.18
Volume ratio (%)	Type 1 fraction	1.5
	Type 2 fraction	2.0

Note: For superplasticizer, S/P ratio indicates the weight ratio of superplasticizer to paste material (including cement, silica fume, and fly ash). For water, W/P ratio indicates the weight ratio of water to paste material (including cement, silica fume, and fly ash). For steel fibers, Type 1 denotes steel fibers with diameter (D) = 0.12 mm and length (L) = 8 mm. Type 2 denotes steel fibers with D = 0.2 mm and L = 13 mm.

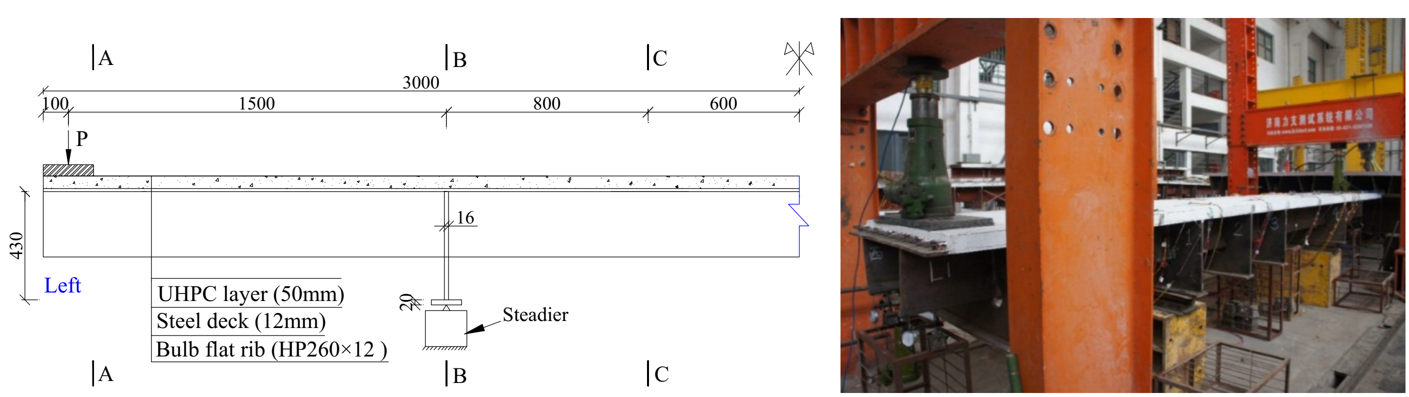

Fig. 17. Test setup scheme and photograph (all dimensions are in millimeters) (Note: UHPC = ultrahigh-performance concrete)

J. Bridge Eng., 2016, 21(7): 04016039

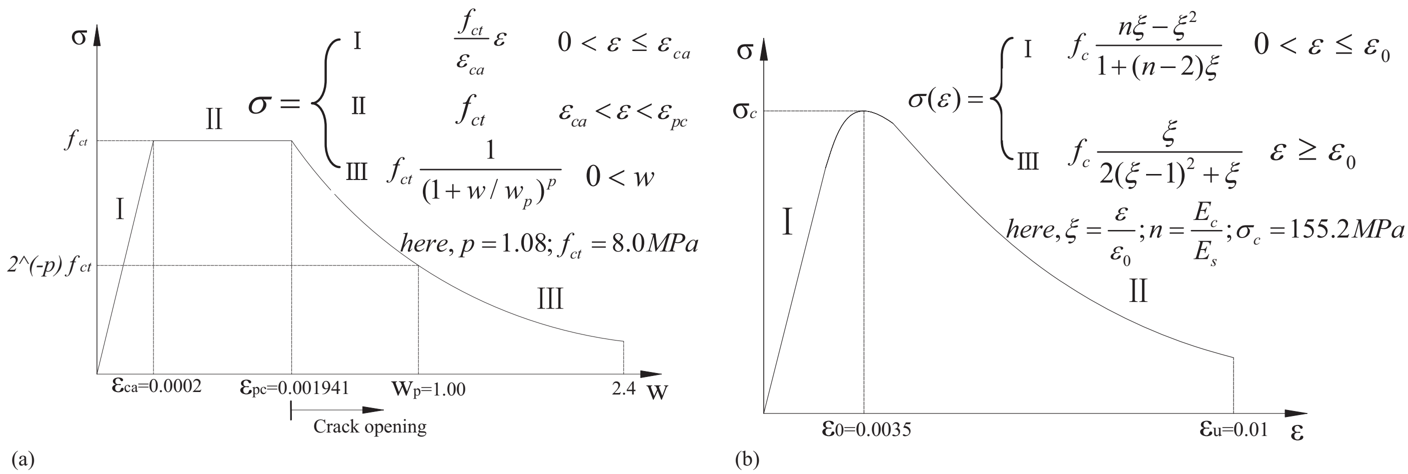

Fig. 18. Stress–strain relationship of ultrahigh-performance concrete: (a) tension; (b) compression (Note: ε_{ca} = first cracking strain; f_{ct} = first cracking stress; ε_{pc} = limit strain; E_s = initial elastic module; E_c = secant elastic module at peak point)

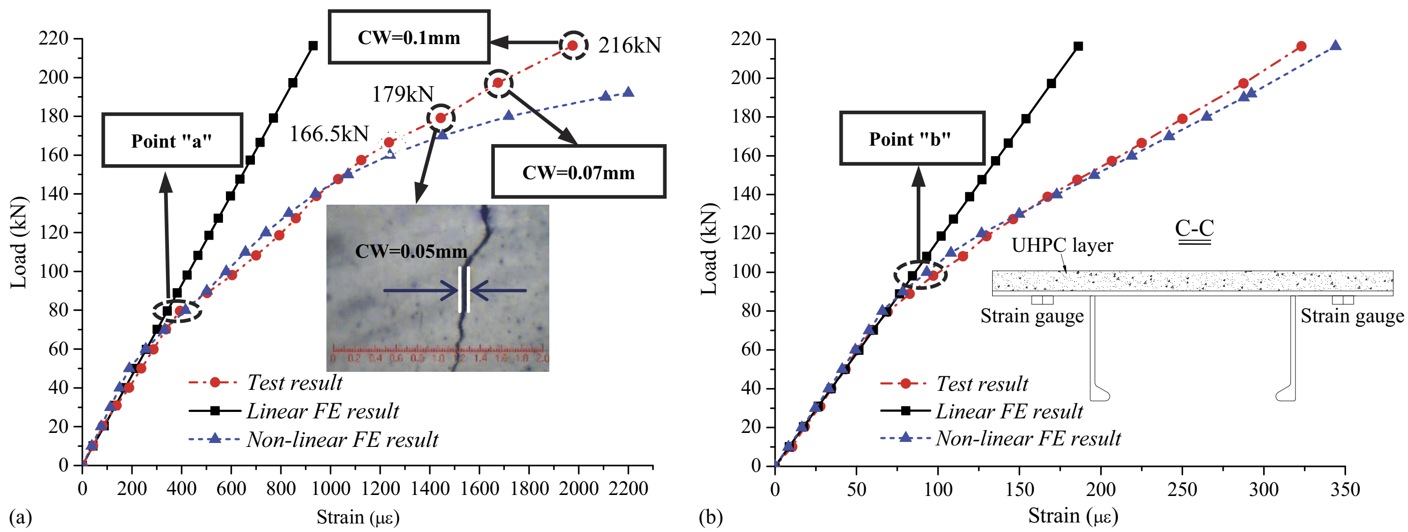

Fig. 19. Result comparison: (a) load–strain curve of ultrahigh-performance concrete at Section B–B; (b) load–strain curve of deck plate at Section C–C (Note: FE = finite element; UHPC = ultrahigh-performance concrete; CW = crack width)

which provides more material models for concrete, including strain-hardening behavior.

For the nonlinear FE model, the steel plates were modeled by shell elements (S4R), the UHPC layer was modeled by solid elements (C3D8R), and the steel reinforcement bars were modeled by the embedded beam elements (B31). Material nonlinearity was considered for both the UHPC and the steel. For the UHPC, the stress–strain relationship in tension used the model proposed by Zhang et al. (2015), as shown in Fig. 18(a), and the stress–strain relationship in compression used the model proposed by Yang (2007), as shown in Fig. 18(b). The steel was assumed to possess an ideal plastic–elastic behavior in both tension and compression. Considering that the internal forces in studs were low, the analysis did not consider slips at the UHPC–OSD interface.

The results are shown in Fig. 19, in which "linear FE result" represents the results obtained from the *ANSYS* linear FEA, "nonlinear FE result" represents the results obtained from the *Abaqus* nonlinear FEA, and "test result" represents the test results.

Table 4. Peak Tensile Stresses of the Ultrahigh-Performance Concrete in the Second Dongting Lake Bridge

	Tensile stresses (MPa)		
Stress direction	Global	Local	Total
Longitudinal	9.90	7.91	17.81
Transverse	—	10.95	10.95

According to Figs. 19(a and b), the turning points are obvious in the load–strain curves. When the load was below the turning points, the three load–strain curves agreed well with each other; when the load exceeded the turning points, the nonlinear phenomenon became apparent. The load level at which the turning points appeared for Fig. 19(a) was approximately 80 kN (Point a), and that for Fig. 19(b) was approximately 100 kN (Point b). In general, the FE results, for which the material nonlinearity was taken into account, are closer to the test results.

This comparison reveals that, if the UHPC layer behaves at a low stress level, it is reasonable to take into account only linear elastic behavior for the UHPC. This assumption is especially important for FE analysis in the section titled "FEA," in which the finite-element models have numerous elements and nodes, and multiple load cases should be taken into account to obtain the stress history of the OSD. These factors make the FEA prohibitive if nonlinear analysis is to be considered. Thus, the FEA in the section titled "FEA" took into account only the linear elastic properties of UHPC.

According to the FEA in this paper, the maximum tensile stress of the UHPC layer in FE Model 1 was 10.95 MPa (Table 4), and the corresponding strain was 10.95 MPa/42.6 GPa = 257 $\mu\varepsilon$. According to Fig. 19(a), when a load level of 59.9 kN was applied, the tested strain in the UHPC layer was 287 $\mu\varepsilon$, which is slightly greater than 257 $\mu\varepsilon$. Thus, the results at this load level were selected for comparison. By comparing the linear elastic results with the test results, the difference was 1 – 258/287 = 10.1%, whereas by comparing the nonlinear results with the test results, the difference was 1 – 255/287 = 11.1%. It can be seen that at this load level, the predicted result based on the linear elastic analysis was quite close to the result derived from the nonlinear analysis. The results obtained from the linear elastic analysis had a maximum difference of 10.1% relative to the test results. Thus, the linear elastic results should be acceptable. However, the linear elastic assumption for the UHPC is acceptable only if the UHPC layer is at a low stress level. Otherwise, the material nonlinear performance of UHPC should be considered.

In addition, the test results shown in Fig. 19(a) revealed that under a load level of 166.5 kN, the UHPC layer was still intact, and the first visible crack developed at a load level of 179.0 kN. According to the linear FEA results presented in Fig. 19(a), the nominal tensile stress of the UHPC layer under the load of 166.5 kN was 30.5 MPa. Such tensile stress was deemed the nominal tensile strength of the UHPC, i.e., f_{tm} = 30.5 MPa.

Fatigue Evaluation for UHPC

Another essential concern relative to the LWCD is the fatigue performance of the UHPC layer, which is discussed in this subsection.

Although many studies have been conducted on the fatigue of ordinary concrete, only a few studies have been undertaken for UHPC, especially on the tension performance of UHPC. Behloul and Chanvillard (2005) performed fatigue tests on 3-point flexure bending specimens for UHPC. The upper and lower fatigue loads were 90 and 10% of the elastic limit load of the specimens, respectively. The tests revealed that the specimens exhibited no obvious damage after experiencing 1 million cycles of loading. Farhat et al. (2007) tested the fatigue performance of UHPC through 3-point flexural specimens. They concluded that at a fatigue endurance of 1 million cycles, small-scale specimens have stable fatigue strength, which is 0.85 times the static flexural strength. However, large-scale specimens exhibited relatively large scatter. Parant et al. (2007) performed 4-point flexural bending fatigue tests for UHPC and found that the fatigue strength of UHPC at 2 million cycles was 0.65 time its static strength. Lappa (2007) obtained the *S–N* curves of UHPC from flexural fatigue tests and concluded that the *S–N* curves of normal concrete also apply to high-strength and ultrahigh-strength concrete, which would lead to conservative results. Makita and Brühwiler (2014) undertook comprehensive research to reveal the fatigue performance of both plain UHPC and UHPC reinforced with steel bars. The tests revealed that stress distribution and transfer between UHPC and steel rebar enhanced the fatigue capacity of both material components.

On the basis of the calculation results of FE Model 1 in the section titled "Parametric Studies," the local tensile stresses of the UHPC were obtained. However, a global finite-element model was built by Ouyang et al. (2014) for the SDTL Bridge to capture the global tensile stresses in UHPC, which considered a dead load and six-lane traffic loads. Table 4 summarizes the results.

Ding and Shao (2015) performed fatigue tests on an OSD–UHPC composite beam model to reveal its behavior in negative bending. In the fatigue tests, the equivalent tensile stress range of the UHPC layer was 0.0–21.30 MPa. The term "equivalent tensile stress range" denotes an impulse stress range that causes identical fatigue damage to the UHPC as the applied stress ranges in the test. The concept of equivalent tensile stress range is based on the fact that different stress ranges can cause identical fatigue damage to a material. The test results indicate that the UHPC layer remained intact, and no fatigue cracks developed after experiencing 3.1 million cycles of loading. The cracks are defined as visible macrocracks, which have a width of 0.05 mm. According to Table 4, the stress range of the UHPC layer can be assumed to be 0.00–17.81 MPa. Thus, the UHPC layer to be used on the SDTL Bridge should also safely resist cyclic traffic loads because the predicted stress range under the design loads is less than 21.3 MPa.

Cao et al. (2015) performed a fatigue assessment for the UHPC layer of a LWCD pilot project in China for the Mafang Bridge. The assessment was based on an *S–N* curve of ordinary concrete in tension (Song 2006), as shown in Eq. (2).

$$\log_{10} N = 16.67 - 16.76\frac{\sigma_{\max}}{f_{\mathrm{tm}}} + 5.17\frac{\sigma_{\min}}{f_{\mathrm{tm}}} \tag{2}$$

where N = fatigue life of ordinary concrete; $\sigma_{\max}$ = maximum tensile stress in concrete (in MPa); $\sigma_{\min}$ = minimum tensile stress in concrete (in MPa); and f_{tm} = static tensile strength of concrete (in MPa).

By substituting $\sigma_{\min}$ = 0 MPa, $\sigma_{\max}$ = 17.81 MPa, and f_{tm} = 30.5 MPa in Eq. (2), the fatigue life of the UHPC layer is estimated to be $N = 7.6 \times 10^6$ cycles, a value much greater than 2 million cycles.

As stated by Cao et al. (2015), the *S–N* curve of ordinary concrete is used for UHPC because, according to investigations by Lappa (2007), although UHPC has superior static strength, its fatigue performance is not appreciably different from that of ordinary concrete.

Conclusions

This paper proposes a novel LWCD that is composed of an open-ribbed OSD and a thin UHPC layer and illustrates its excellent fatigue performance via FEA and fatigue tests. On the basis of the current investigations, the following conclusions can be drawn:

1. FEAs and fatigue tests revealed that all of the components of the open-ribbed LWCD, including the OSD, headed studs, and UHPC layer, possess high fatigue endurance. In addition, the open-ribbed OSD within the LWCD is easier to fabricate than a conventional U-ribbed OSD. Thus, the open-ribbed LWCD provides a competitive solution for minimizing the fatigue cracking risk in OSD bridges.
2. Preliminary FEA results revealed that the vehicle-induced stress ranges of six typical fatigue details in the open-ribbed LWCD are reduced by 35.1 to 87.3% compared to the stress ranges in conventional OSDs. As a consequence, the stress ranges of the rib–deck plate welds, as well as the splice welds in the ribs in the LWCD, are below their corresponding

CAFLs, which indicates a theoretically infinite fatigue life of these fatigue details. However, the stress ranges at the free edge of the cutouts are still above the CAFLs. Thus, special attention should be paid to this fatigue detail in design.

3. Detailed parametric studies were performed for the LWCD to gain deeper insight into the fatigue behaviors of fatigue details at the rib–floor beam welded joints and the free edge of the cutouts. Two parameters were considered, namely, the shape of the cutouts and thickness of the floor beams. The analyses show that the apple-shaped cutout (Cutout 3) has relative low stress ranges compared to those of the other three. Furthermore, it is beneficial to increase the thickness of the floor beams 14–18 mm; in this case, the stress ranges in all of the six fatigue details are less than their CAFLs.
4. A fatigue test was carried out on a LWCD panel specimen, which was loaded by cyclic negative bending moments. The most unfavorable fatigue detail of the specimen was found to be the free edge of the cutout, which had a stress range of 90.6 MPa. After experiencing 2.5 million cycles of loading, the specimen developed no fatigue cracks.
5. Another fatigue test was conducted on an OSD–UHPC composite beam specimen to explore the fatigue characteristics of the stud shear connectors embedded in UHPC. The test used fatigue loads with variable amplitude, which produced a maximum shear stress range of 35.5 MPa (for 2.0 million cycles) and 77.4 MPa (for 2.25 million cycles) in the studs, respectively. No fatigue failure was detected in the studs. Considering that the maximum predicted stress range of the studs under the design load is 48.8 MPa, the number of loading cycles before fatigue failure by following Miner's rule can be estimated to be 90 million, a value much greater than 2 million.

Acknowledgments

This research was supported by the National Natural Science Foundation of China (51178177) and the Transportation Science and Technology Major Project sponsored by the Ministry of Transport of China (2011318494160). These programs are gratefully acknowledged.

References

Abaqus 6.14 [Computer software]. Dassault Systèmes, Waltham, MA.

ANSYS 14.0 [Computer software]. ANSYS, Canonsburg, PA.

Aygül, M., Al-Emrani, M., and Urushadze, S. (2012). "Modelling and fatigue life assessment of orthotropic bridge deck details using FEM." *Int. J. Fatigue*, 40, 129–142.

Behloul, M., and Chanvillard, G. (2005). "Fatigue flexural behavior of pre-cracked specimens of special UHPFRC." *Proc., Seventh Int. Symp. on the Utilization of High Strength/High-Performance Concrete*, American Concrete Institute, Farmington Hills, MI.

Cao, J. H., Shao, X. D., Zhang, Z., and Zhao, H. (2015). "Retrofit of an orthotropic steel deck with compact reinforced reactive powder concrete." *Struct. Infrastruct. Eng.*, 12(3), 411–429.

Chen, B., Zhong, Z., Xie, X.,Wang, J. W., and Lu, P. Z. (2014). "Site-specific fatigue load spectrum for urban bridges." *14th COTA Int. Conf. of Transportation Professionals*, ASCE, New York, 1051–1060.

Connor, R. J. (2004). "Influence of cutout geometry on stresses at welded rib-to-diaphragm connections in steel orthotropic bridge decks." *Transportation Research Board*, 1892, 78–87.

Connor, R. J., and Fisher J. W. (2006). "Consistent approach to calculating stresses for fatigue design of welded rib-to-web connections in steel orthotropic bridge decks." *J. Bridge Eng.*, 10.1061/(ASCE)1084-0702(2006)11:5(517), 517–525.

Ding, N., and Shao, X. D. (2015). "Study on fatigue performance of light-weighted composite bridge deck." *China Civ. Eng. J.*, 48(1), 74–81 (in Chinese).

ECS (European Committee for Standardization). (2003). "Eurocode 1: Actions on structure—Part 2: Traffic loads on bridges." *EN 1991-2*, Brussels, Belgium.

ECS (European Committee for Standardization). (2004). "Eurocode 4: Design of composite steel and concrete structures—Part 1-1: General rules and rules for buildings." *EN 1993-1-1*, Brussels, Belgium.

ECS (European Committee for Standardization). (2005). "Eurocode 3: Design of steel structures—Part 1-9: Fatigue." *EN1993-1-9*, Brussels, Belgium.

Erzurumlu, H., and Toprac, A. A. (1972). "Fatigue of orthotropic bridge deck." *J. Struct. Div.*, 98(4), 813–830.

Farhat, F. A., Nicolaides, D., Kanellopoulos, A., and Karihaloo, B. L. (2007). "High performance fibre-reinforced cementitious composite (CARDIFRC)—Performance and application to retrofitting." *Eng. Fract. Mech.*, 74(1–2), 151–167.

Fricke, W. (2003). "Fatigue analysis of welded joints: State of development." *Mar. Struct.*, 16(3), 185–200.

Frýba, L., and Gajdos, L. (1999). "Fatigue properties of orthotropic decks on railway bridges." *Eng. Struct.*, 21(7), 639–652.

Hobbacher, A. (2008). *Recommendations for fatigue design of welded joints and component (XIII-2151r4-07/XV-1254r4-07).* Springer International, Cham, Switzerland.

Jong, F. B. P. (2004). "Overview fatigue phenomenon in orthotropic bridge decks in the Netherlands." *Proc., 1st Int. Orthotropic Bridge Conf.*, ASCE, New York, 489–512.

Lappa, E. S. (2007). "High strength fibre reinforced concrete: Static and fatigue behavior in bending." Ph.D. dissertation, Delft Univ. of Technology, Delft, Netherlands.

Li, J., Yang, B., Shao, X. D., and Li, J. (2015). "Shear fatigue performance of studs of composite deck system composed of steel and super toughness concrete layers." *China Civ. Eng. J.* (in Chinese), in press.

Liu, R., Liu, Y. Q., Ji, B. H., Wang, M., and Tian, Y. (2014). "Hot spot stress analysis on rib-deck welded joint in orthotropic steel decks." *J. Constr. Steel Res.*, 97, 1–9.

Makita, T., and Brühwiler, E. (2014). "Tensile fatigue behaviour of ultra-high performance fibre reinforced concrete combined with steel rebars (R-UHPFRC)." *Int. J. Fatigue*, 59(3), 145–152.

Ouyang, Z. H., Zhang, S. H., Shao, X. D., Cao, J. H., Li, Z. H., and Peng B. (2014). "Static and fatigue tests on light-weighted composite bridge deck with open and closed ribs in Dongting Lake Bridge." Dept. of Bridge Engineering, Hunan Univ., Changsha, China, 1–127 (in Chinese).

Parant, E., Rossi, P., and Boulay, C. (2007). "Fatigue behavior of a multi-scale cement composite." *Cem. Concr. Res.*, 37(2), 264–269.

Shao, X. D., Yi, D. T., Huang, Z. Y., Zhao, H., and Chen, B. (2013). "Basic performance of the composite deck system composed of orthotropic steel deck and ultrathin RPC Layer." *J. Bridge Eng.*, 10.1061/(ASCE)BE.1943-5592.0000348, 417–428.

Song, Y. P. (2006). *Fatigue behavior and design principle of concrete structures.* China Machine Press, Beijing (in Chinese).

Tang, L., Huang, L. J., Wang, X. W., and Liu, G. (2014). "Analysis of stress in U-rib-diaphragm joints of steel deck." *J. Highway Transp. Res. Dev.*, 31(5), 93–101 (in Chinese).

Wolchuk, R. (1999). "Steel orthotropic decks: Developments in the 1990s." *Transportation Research Board*, 30–37.

Wolchuk, R., and Ostapenko, A. (1992). "Secondary stresses in closed orthotropic deck ribs at floor beams." *J. Struct. Eng.*, 10.1061/(ASCE)0733-9445(1992)118:2(582), 582–595.

Xiao, Z. G., Yamada, K., Ya, S., and Zhao, X. L. (2008). "Stress analyses and fatigue evaluation of rib-to-deck joints in steel orthotropic decks." *Int. J. Fatigue*, 30(8), 1387–1397.

Yang, J. (2007). "Flexural behavior of ultra-high performance concrete beams prestressed with CFRP tendons." Ph.D. dissertation, Hunan Univ., Changsha, China (in Chinese).

Zhang, B. (2011). "Research on structural behavior of orthotropic deck with open-shaped ribs of steel truss bridge." Master dissertation, Tianjin Univ., Tianjin, China (in Chinese).